Ultrabroadband and Reconfigurable Transmissive Acoustic Metascreen

Xudong Fan, Yifan Zhu, Zihao Su, Ning Li, Xiaolong Huang, Yang Kang, Can Li, Chunsheng Weng, Hui Zhang, Bin Liang, et al.

Ultrabroadband and Reconfigurable Transmissive Acoustic Metascreen

Xudong Fan Yifan Zhu Zihao Su Ning Li Xiaolong Huang Yang Kang Can Li Chunsheng Weng Hui Zhang* Bin Liang* Badreddine Assouar**

Prof. X. Fan, Prof. N. Li, Prof. X. Huang, Prof. Y. Kang, Prof. C. Li, Prof. C. Weng
National Key Laboratory of Transient Physics, Nanjing University of Science and Technology, Nanjing 210094, China
Email Address: fanxudong@njust.edu.cn
Prof. Y. Zhu, Z. Su, Prof. H. Zhang
Jiangsu Key Laboratory for Design and Manufacture of Micro-Nano Biomedical Instruments, School of Mechanical Engineering, Southeast University, Nanjing 211189, China
Email Address: seuzhanghui@seu.edu.cn
Prof. B. Liang
Collaborative Innovation Center of Advanced Microstructures and Key Laboratory of Modern Acoustics, MOE, Institute of Acoustics, Department of Physics, Nanjing University, Nanjing 210093, China
Email Address: liangbin@nju.edu.cn
Prof. B. Assouar
Université de Lorraine, CNRS, Institut Jean Lamour, F-54000 Nancy, France
Email Address: badreddine.assouar@univ-lorraine.fr

Keywords: *Acoustic metamaterials, Reconfigurable acoustic metascreen, Ultrabroad frequency band, Transmitted sound manipulations*

Passive acoustic wave manipulations are severely constrained by the narrow frequency bandwidth of acoustic metastructures. In this research, we propose an unprecedented type of reconfigurable acoustic metascreen for broadband manipulations of transmitted acoustic waves. The conceived structure is composed of uniquely designed unit cells producing the modulation of the transmitted phase shift within the full 2π range with an excellent impedance matching with the background medium. By rationally arranging the reconfigurable elements within the metascreen based on the corresponding parameter profile, different phenomena and functionalities can be easily realized. As examples, acoustic focusing and acoustic bending are presented to showcase the performance of the proposed metascreen. We indeed numerically and experimentally demonstrate the ultra-broadband and reconfigurable features of our concept over an astonishing frequency range extending from 3 to 17 kHz, which covers the majority spectrum of the audible range of human hearing. Our work provides a unique and remarkable conceptual design of acoustic metascreen opening a promising and pragmatic route to conceive compact broadband acoustic devices, where wavefront manipulations on broadband sound signals or pulsed signals are required.

1 Introduction

Precise control of propagating acoustic waves is critical in acoustic research and finds many applications such as medical imaging/therapy, noise control, and acoustic communications. Conventional methods usually use natural materials with some specific acoustic properties, which could modulate the phase of propagating waves gradually, and in turn, manipulate the sound wavefront. However, the inherent bulky size and irregular geometry of conventional acoustic structures are inconvenient in many situations, and therefore, limit their applications. Another common method would be using active phased array systems. The phase of each transducer within the phased array must be tuned individually, which will inevitably cause complexity and a high cost for the working system.

In the past decade, wavefront manipulations based on compact passive structures, so-called acoustic metamaterials, have attracted increasing interest. Acoustic metamaterials and metasurfaces can provide additional phase shifts and in hence can manipulate acoustic wavefronts directly based on Fermat's principle. [1, 2, 3, 4, 5, 6, 7, 8, 9, 10, 11, 12, 13, 14, 15, 16, 17] Great efforts have been made in regard of the development of acoustic metamaterials and metasurfaces, and extraordinary acoustic phenomena have been realized such as negative refraction or reflection, [18, 19] acoustic one-way propagation, acoustic cloaking, [20] acoustic imaging, [21] acoustic hologram, [22, 23] and vortex field generation. [24]

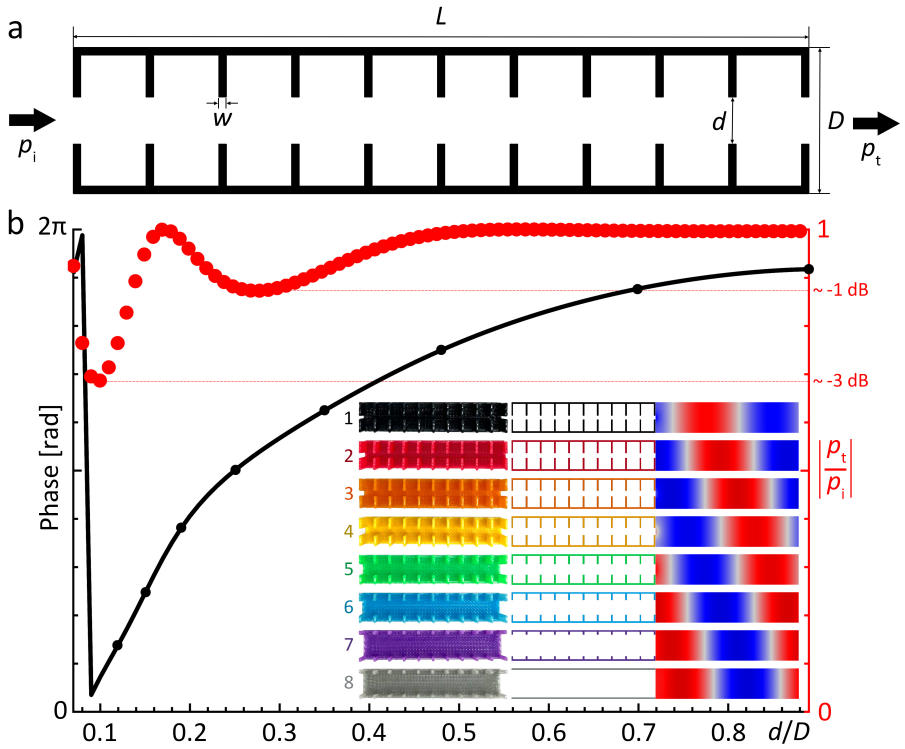

Figure 1: (a) Illustration of a single element in x-y plane. (b) The transmission rate $|p_t/p_i|$ (the red dots) and phase shift (the black solid line) of the simulated field at the frequency of 5700Hz. Inset: the patterns of transmitted acoustic pressure field of the eight elements, corresponding to the eight black dots in the black solid curve of the phase shift.

Although significant progress has been made in the study of acoustic metamaterials, the current structures are still restricted by the unicity of working frequency. In addition, in most cases, the structure sample is fabricated as a whole piece, which is applicable only to a single function and cannot be reconfigured. These deficiencies cannot fulfill the application requirements for flexible and complex acoustic field manipulations within a broad frequency band. In recent years, great effort has been made in regard to the reconfigurable acoustic metamaterials of different forms, [25, 26, 27, 28, 29, 30, 31, 32, 33, 34, 35, 36] which provides inspiring ideas to solve the limitation of unchangeable structures. There are also few studies focusing on broadband sound manipulations. [37, 38, 39] However, they either only work for reflected waves [4, 9, 39, 40] or on a narrow frequency range. Hence, flexible and broadband transmitted wave manipulations using reconfigurable acoustic metastructure are still highly desired.

In this paper, we propose a new type of reconfigurable acoustic metascreen for the broadband manipulation of transmitted acoustic waves. The reconfigurable acoustic structure consists of a straight channel as a base decorated with a series of length-varying straight barriers as pluggable elements. The structure proposed here is unique and very simple, capable to fully modulate the transmitted phase shifts within 2π span while keeping a high transmission rate. With the advantage of simple design and easy fabrication, the metascreen could manipulate the transmitted wavefront precisely and flexibly within a remarkable ultra-broadband frequency range. The working frequency band from 3 to 17 kHz covers a large part of the audible range of human hearing, which outperforms most of the previous works due to the novel geometry design and the different physical mechanisms of this work. The conceived structure here provides us the flexibility to re-arrange the reconfigurable elements within the metascreen based on the corresponding parameter profile so that different phenomena and functionalities can be easily realized. To showcase the performance of our metascreen, the phenomena of acoustic focusing and acoustic bending are demonstrated as examples, where the simulated and experimental results are consistent with the expectations, and also proving the reconfigurable and ultra-broadband features of the metascreen. Our research opens a promising avenue to design and develop simplified ultra-broadband acoustic devices based on metamaterials for real applications.

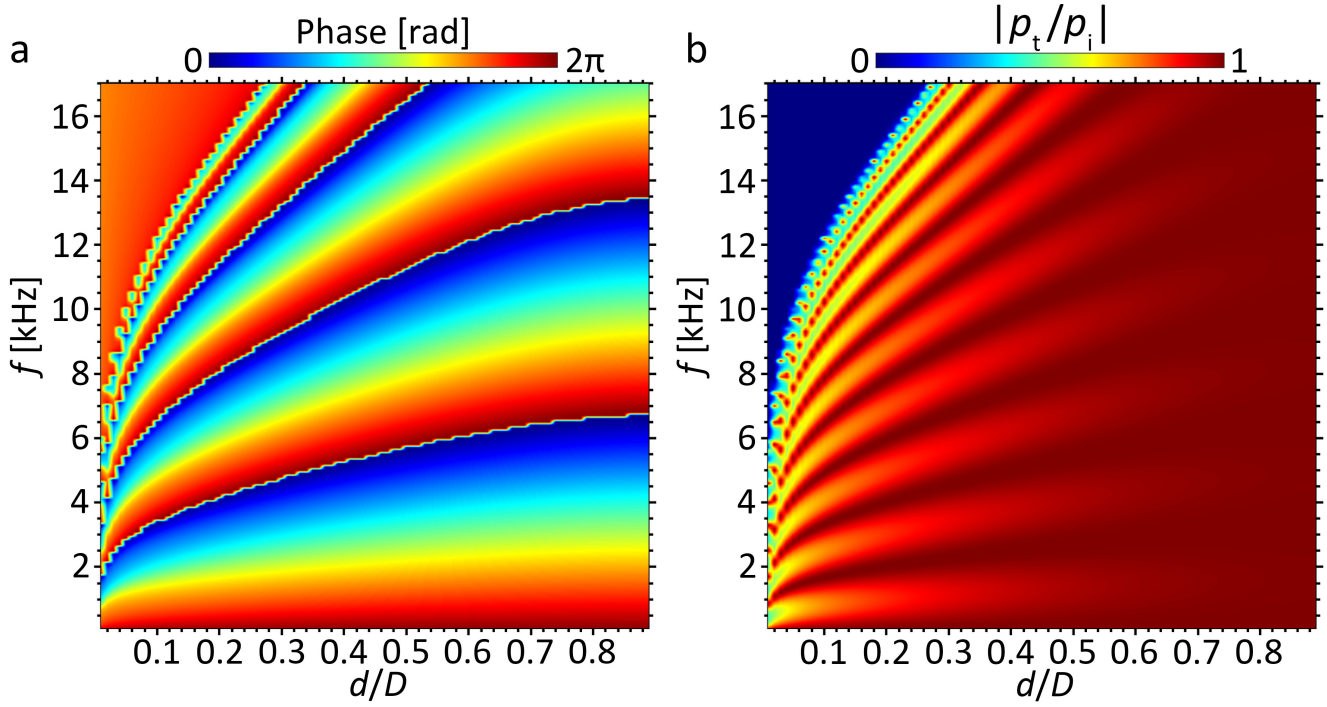

Figure 2: (a) Phase shift and (b) transmission rate $|p_t/p_i|$ when varying the frequency f and the geometry parameter d/D.

2 Results

2.1 Ultra-broad band transmissive metascreen: model and design

A single element of the acoustic metascreen proposed here is illustrated in Fig. 1(a) as an example, where the element with the width D is constructed by a straight channel decorated with a series of length-varying straight barriers of the same thickness w. The total length of the structure is designed as $L = 50$ mm and the width is $D = 10$ mm. The wall thickness of the whole structure is $w = 0.5$ mm. The opening width d is varied to change the structure and in turn control the transmitted field.

To examine the dependence of the transmitted field on the geometrical parameters of the structure element, we numerically simulate the transmitted acoustic field through the structure. The incident frequency is set to 5700 Hz, which corresponds to the wavelength of $\lambda \sim 60$ mm. Numerical results of the phase shift and corresponding transmission rate $|p_t/p_i|$ of the transmitted sound field are shown in Fig. 1(b), where p_i and p_t are the incident and transmitted sound pressures. From the results, the transmitted phase shift (black solid line) can cover the span of 2π when varying the geometry parameter d/D, while keeping the transmission rate (red dots) at a high level ($>\sim -3$ dB). This indicates that most of the energy can pass through the structure, and the transmitted wavefront can be modulated at will.

To clearly illustrate the transmitted field, simulated phase fields for eight different types of elements are shown in the inset in Fig. 1(b), where the phase shift of 2π range is covered with the interval of $\pi/4$. The parameters d/D of the eight elements are 0.12, 0.15, 0.19, 0.25, 0.35, 0.48, 0.70, 0.90, respectively, corresponding to the eight black points in Fig. 1(b).

We further examine the broadband property of the structure proposed here by varying both the geometrical parameter d/D and the working frequency f of the incident sound waves. The corresponding results for the phase shift and the transmission rate in the parameter space $(d/D, f)$ are shown in Fig. 2(a) and (b), respectively. From the results, the tendency of the phase shift is quite similar within the majority part of the audible range of human hearing while keeping the transmission rate at a high level. The broadband property shown here indicates that the structure proposed can solve the narrow-band challenge encountered by some other structures, and realize desired acoustic phenomena in an ultra-broadband frequency bandwidth.

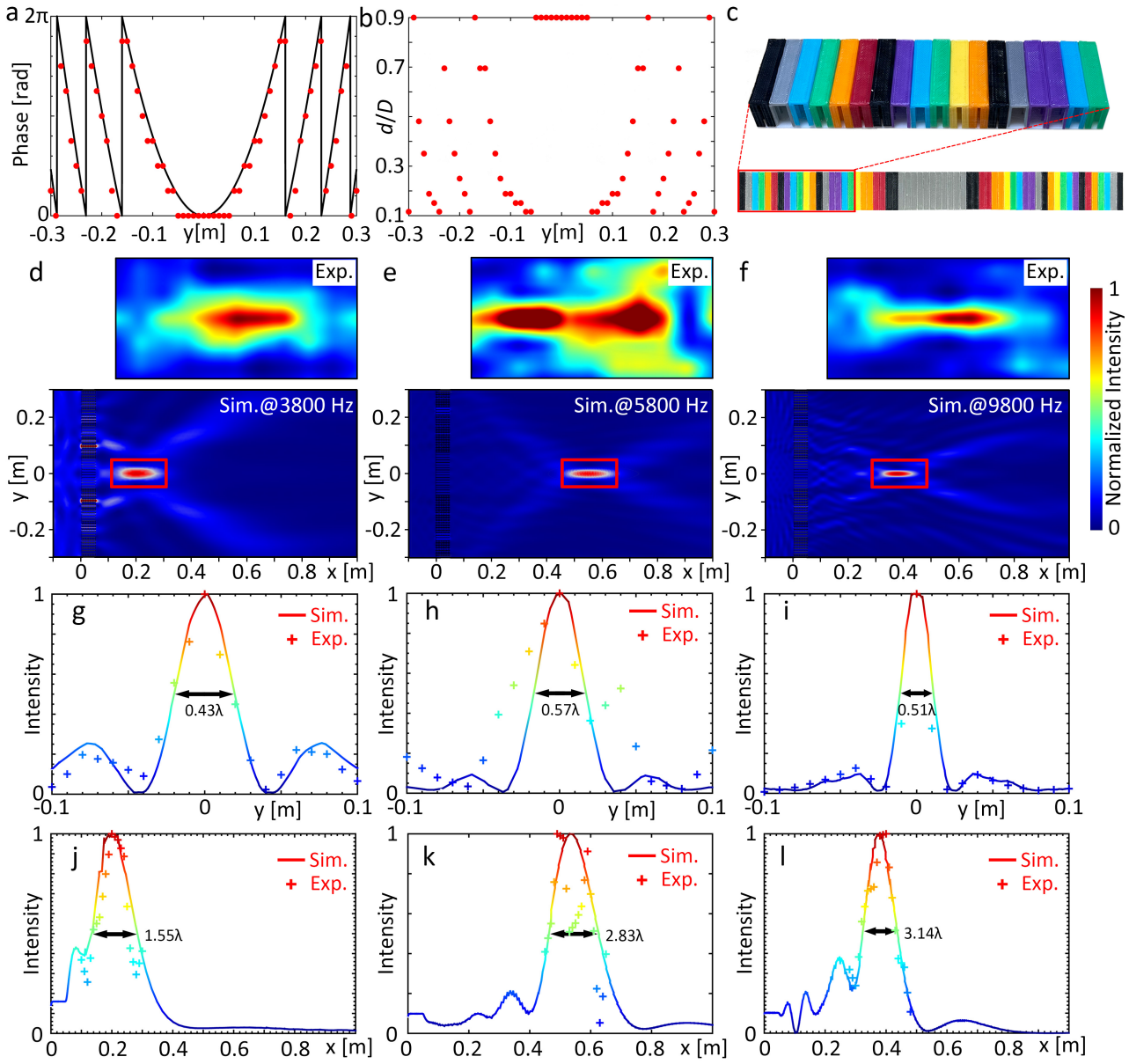

Figure 3: Ultra-broadband acoustic focusing. (a) Continuous (black solid line) and discrete phase shift (red dots) and (b) corresponding discrete geometry parameters for the phenomenon of acoustic focusing. (c) Sample photo of the metascreen. (d-f) Measured and simulated intensity fields for acoustic focusing at the frequencies of 3800 Hz, 5800 Hz, and 9800 Hz. (g-i) Measured and simulated intensity profiles in the transverse y direction near the focal regions. (j-l) Measured and simulated intensity profiles in the x direction near the focal regions.

2.2 Acoustic focusing

To illustrate the ultra-broadband performance of the structure proposed here, we first demonstrate the phenomenon of acoustic focusing using the acoustic metascreen. The phase profile, $\Phi(y)$, on the interface between the acoustic metascreen and the background medium should satisfy the generalized Snell's law of refraction, [18] i.e.,

$$\sin\theta_t - \sin\theta_i = \frac{\lambda}{2\pi}\frac{d\Phi(y)}{dy} \tag{1}$$

where θ_i and θ_t are the incident and refraction angles, respectively.
For the acoustic focusing, the phase gradient along the metascreen $d\Phi(y)/dy$ varies with the spatial location y, and the phase profile along the interface should satisfy [18]

$$\Phi(y) = \frac{2\pi}{\lambda}\Big[(\sqrt{y^2+f^2}-f) + (\sqrt{y^2+x_s^2}-|x_s|)\Big], \tag{2}$$

where f is the focal length, and the second term within the square brackets characterizes the phase correction from a loudspeaker located at $(x_s, 0)$. The phase profile provided by the metascreen for acoustic focusing is shown in Fig. 3(a), where the black solid line indicated the continuous phase profile characterized by Eq. (2) and the red points exhibits the discrete phases of 100 elements. Here, we choose $f = 0.5$ m and $x_s = -0.35$ m as an example. The corresponding geometry parameters of the metascreen are shown in Fig. 3(b). The sample photo is shown in Fig. 3(c), where the acoustic metascreen consists of a common base inserted by eight different types of elements (indicated by eight colors); see Inset in Fig. 1(b). The metascreens for different functions and phenomena can be constructed by arranging the eight types of elements based on the corresponding geometry profile and the number order.
In order to demonstrate the broadband property of the metascreen, we numerically simulate the acoustic intensity field transmitted through the structure [Fig. 3(c)] within a wide frequency range. The simulated sound intensity fields for three typical frequencies, i.e., 3800 Hz, 5800 Hz and 9800 Hz, are shown in Fig. 3(d-f), respectively. It is clearly observed that the acoustic metascreen designed here can effectively converge the transmitted energy to the focal point, which is $x = 0.2$ m, 0.55 m, and 0.38 m for the three frequencies, 3800 Hz, 5800 Hz, and 9800 Hz, respectively. The acoustic energy in the other regions is much weaker than that in the focal region. To confirm the broadband performance of the designed acoustic metascreen, we measure the transmitted acoustic fields in the scan areas bounded by the red rectangle boxes. The measured fields agree well with the simulated results, proving the ultra-broadband features of the metascreen in our design.
To quantitatively examine the performance of the structure, the normalized intensity distributions along the transverse y cross-section at the focal point are characterized in Fig. 3(g-i). The full widths at half maximum height (FWHM) of the sound intensity for the three frequencies are 0.43λ, 0.59λ, and 0.51λ. In addition, the normalized intensity distributions along the axial direction at $y = 0$ for the three frequencies are shown in Fig. 3(j-l), where the lengths of the focal region are 1.55λ, 2.83λ, and 3.14λ. We also compare the experimental profile of the intensity field (pluses) with the simulated ones (solid lines), and both results show the excellent bandwidth of focusing effect obtained with our designed metascreen. See Fig. 4 for the schematic diagram of the experimental setup.
The acoustic metascreen exhibits excellent performance for ultra-broadband acoustic focusing. However, the focal intensity and the focal location vary with the working frequency. Figure 5 shows the location and the corresponding intensity amplification at the focal point within the frequency range from 3 kHz to 17 kHz, where the amplification is obtained by the transmitted intensity at the focal point divided by the incident sound intensity. From the results, the focal location increases with frequency pseudo-periodically, and the intensity amplification at the focal location is much larger than 1 within the majority part of the audible range of human hearing, which further confirms the excellent ultra-broadband features of the acoustic metascreen proposed here.

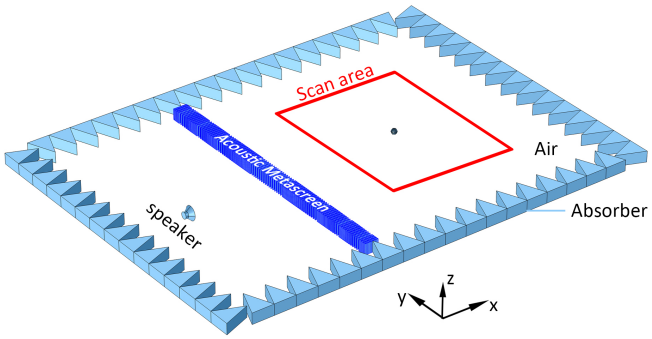

Figure 4: Schematic diagram of the experimental setup. The speaker is located at $(-0.35\ m, 0)$.

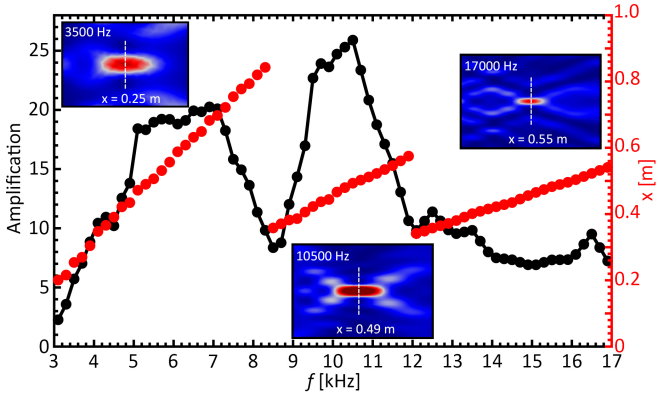

Figure 5: Numerical results of amplification and location of the focal point for different frequencies. Insets: simulated acoustic intensity fields in the focal region for 3500Hz, 10500Hz, and 17000 Hz.

2.3 Acoustic bending

To examine the reconfigurable feature of the acoustic metascreen, we further demonstrate another phenomenon, acoustic bending, using the acoustic metascreen. For an arbitrary trajectory $y = y(x)$, the phase gradient along the interface should satisfy [18]

$$\frac{d\Phi(y)}{dy} = \frac{2\pi}{\lambda}\frac{y'(x)}{\sqrt{1+(y'(x))^2}}, \tag{3}$$

where $y'(x)$ is the slope of the trajectory $y(x)$. The trajectory $y = \sqrt{r^2-(x-r)^2}$ is chosen as an example, which gives the phase profile along the metascreen,

$$\Phi(y) = \frac{2\pi}{\lambda}\left[(y - 2r\sqrt{y/r}) + (\sqrt{y^2+x_s^2} - |x_s|)\right]. \tag{4}$$

The discrete phase profile for $r = 0.35$ m along the metascreen is shown in Fig. 6(a) with the corresponding geometry parameters shown in Fig. 6(b). For this case, the acoustic metascreen is re-constructed by re-arranging the reconfigurable elements based on the new profile and the new number order. The corresponding sample photo is shown in Fig. 6(c).
To demonstrate the broadband property of the metascreen, we examine the acoustic intensity field transmitted through the structure in Fig. 6(c) within a wide frequency range. The measured and simulated sound intensity fields for the same three frequencies, i.e., 3800 Hz, 5800 Hz, and 9800 Hz, are shown in Fig. 6(d-e), respectively, where the transmitted wave bends after passing through the structure as expected. Consequently, the ultra-broadband bending effect is also obtained with the proposed reconfigurable acoustic metascreen, and again confirms the ultra-broadband and reconfigurable features of our designed metascreen.

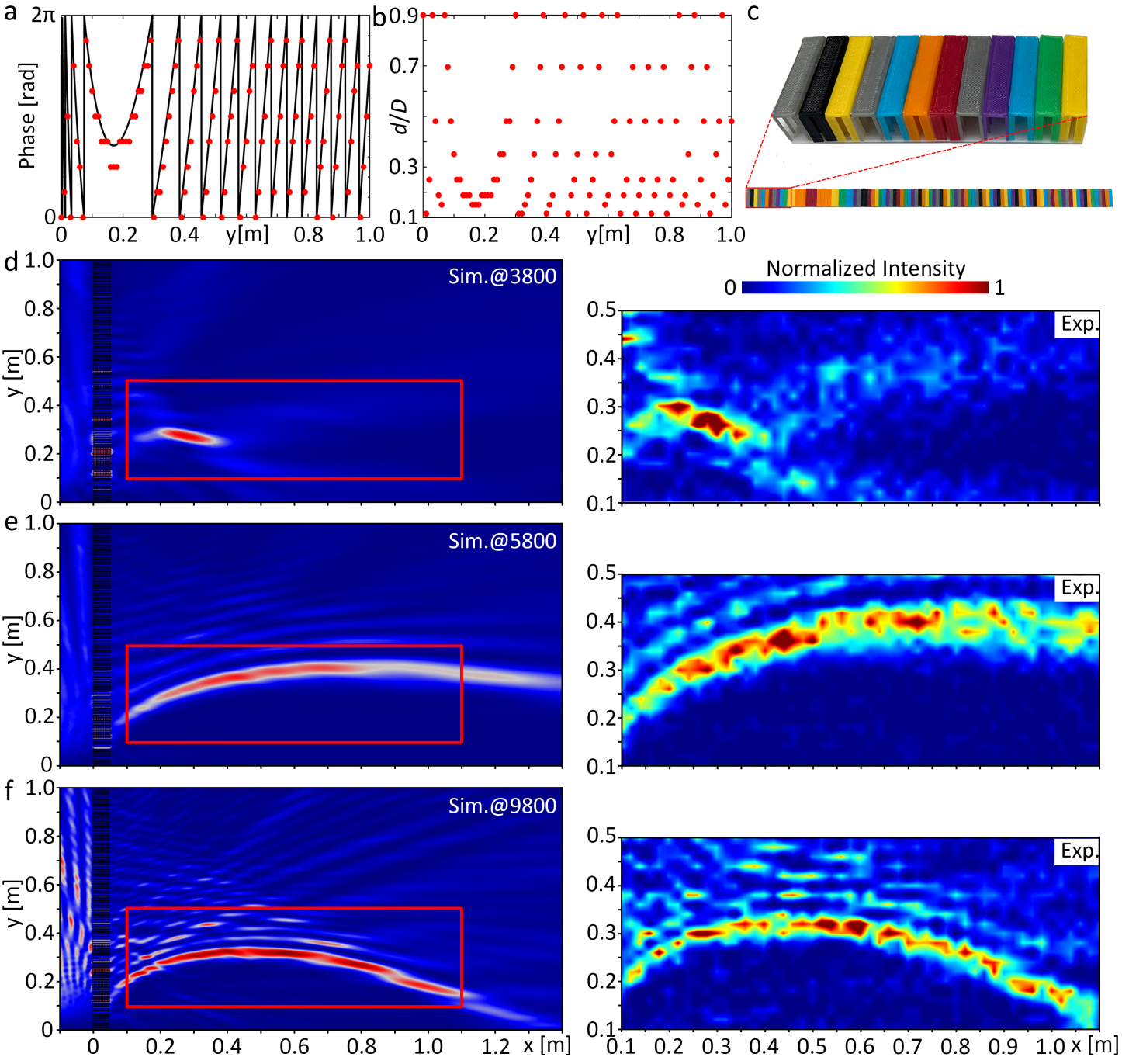

Figure 6: Ultra-broadband acoustic bending. (a) Continuous (black solid line) and discrete phase shift (red dots) and (b) corresponding discrete geometry parameters of the metascreen for the phenomenon of acoustic bending. (c) Sample photo of the metascreen. (d-f) Measured and simulated intensity fields for acoustic bending at the frequencies of 3800 Hz, 5800 Hz, and 9800 Hz.

3 Conclusion

In this paper, a new type of reconfigurable acoustic metascreen for the manipulation of transmitted acoustic waves is proposed and demonstrated. The simple design of the metascreen consists of a straight channel as a common base decorated with a series of length-varying straight barriers as pluggable elements. The structure here could fully modulate the transmitted phase shifts within 2π span while keeping a high transmission rate (transmission loss less than 3dB). The designed metastructure can effectively manipulate acoustic waves at the frequency range extending 3 kHz to 17 kHz, which covers a large part of the audible range of human hearing. Different functionalities have been demonstrated by arranging the pluggable elements into the base following the corresponding phase profile. Acoustic focusing and acoustic bending are presented as examples to showcase the ultra-broadband and reconfigurable features of the structure, proving that the metascreen can manipulate the transmitted wavefront within an ultra-broadband frequency bandwidth. Our work paves the way for further research on broadband acoustic metamaterials and can have real implications for applications in many domains including biomedical acoustics, architectural acoustics, noise control, and so on.

4 Experimental Section

Numerical Simulations: The simulations were performed using commercial software based on the finite element method, COMSOL MULTIPHYSICS with the "Acoustic-Thermoviscous Acoustic Interaction, Frequency Domain." The sound speed and the mass density of the structure are adopted as 2278 m s^{-1} and 1100 kg m^{-3} respectively with the corresponding parameters of the background medium, air, as 343 m s^{-1} and 1.21 kg m^{-3}.

Fabrication: The common base and the eight different types of pluggable elements were fabricated using a commercial extrusion-based 3D printer (Wiiboox Four) with the material PLA of different colors. The printing resolution is 0.1mm. The eight elements in the inset in Fig. 1(b) are shown from the top view. The pluggable panels are stretched for 15 mm. These elements are plugged into the common base in different orders based on different phenomena, for example, Fig. 3(b) for acoustic focusing and Fig. 6(b) for acoustic bending.

Experimental Measurements: The experiments were carried out in a rectangular waveguide (Fig. 4). The transmitted acoustic field is measured within a rectangular waveguide bounded by absorbing foams. A loudspeaker with a diameter of 40 mm was fixed at the incident side of the sample at a distance of 3.5 cm. The speaker was connected to a signal generator (RIGOL DG1032) and a power amplifier (CROWN XLi2500) to generate steady sound signals for different frequencies, and a 1/4-inch microphone is used to measure the transmitted acoustic intensity field with a scanning resolution of 1 cm.

Supporting Information
Supporting Information is available from the Wiley Online Library or from the author.

Acknowledgements
This work was supported by the National Natural Science Foundation of China (Grant No. 12204241 and No. 11874110), the Natural Science Foundation of Jiangsu Province (Grant No. BK20220924), and the open research foundation of Key Laboratory of Modern Acoustics, Ministry of Education, Nanjing University.

Conflict of Interest
The authors declare no conflict of interest.

Author Contributions
X.D.F. and Y.F.Z. contributed equally to this work. X.D.F. proposed the idea and performed the theoretical simulations. X.D.F., Y.F.Z. and Z.H.S designed and conducted the experiments. Y.F.Z., Z.H.S and H.Z. fabricated the samples. X.D.F., B.L. and B.A. wrote the manuscript. N.L., X.L.H, Y.K., C.L.

and C.S.W. revised the manuscript. X.D.F., B.L., H.Z. and B.A. guided the research. All authors contributed to data analysis and discussions.

References

[1] Y. Li, X. Jiang, R.-q. Li, B. Liang, X.-y. Zou, L.-l. Yin, J.-c. Cheng, *Physical Review Applied* **2014**, *2*, 6 064002.

[2] K. Tang, C. Qiu, M. Ke, J. Lu, Y. Ye, Z. Liu, *Scientific reports* **2014**, *4*, 1 1.

[3] Y. Xie, W. Wang, H. Chen, A. Konneker, B.-I. Popa, S. A. Cummer, *Nature communications* **2014**, *5*, 1 1.

[4] Y.-F. Zhu, X.-Y. Zou, R.-Q. Li, X. Jiang, J. Tu, B. Liang, J.-C. Cheng, *Scientific reports* **2015**, *5*, 1 1.

[5] Y. Li, X. Jiang, B. Liang, J.-c. Cheng, L. Zhang, *Physical Review Applied* **2015**, *4*, 2 024003.

[6] G. Ma, P. Sheng, *Science advances* **2016**, *2*, 2 e1501595.

[7] S. A. Cummer, J. Christensen, A. Alù, *Nature Reviews Materials* **2016**, *1*, 3 1.

[8] X. Zhu, K. Li, P. Zhang, J. Zhu, J. Zhang, C. Tian, S. Liu, *Nature Communications* **2016**, *7*, 1 1.

[9] X.-D. Fan, Y.-F. Zhu, B. Liang, J. Yang, J.-C. Cheng, *Applied Physics Letters* **2016**, *109*, 24 243501.

[10] Y. Zhu, X. Fan, B. Liang, J. Cheng, Y. Jing, *Physical Review X* **2017**, *7*, 2 021034.

[11] B. Assouar, B. Liang, Y. Wu, Y. Li, J.-C. Cheng, Y. Jing, *Nature Reviews Materials* **2018**, *3*, 12 460.

[12] X. Fan, B. Liang, J. Yang, J. Cheng, *Scientific Reports* **2019**, *9*, 1 1750.

[13] Z. Hou, X. Fang, Y. Li, B. Assouar, *Physical Review Applied* **2019**, *12*, 3 034021.

[14] Y. K. Chiang, S. Oberst, A. Melnikov, L. Quan, S. Marburg, A. Alù, D. A. Powell, *Physical Review Applied* **2020**, *13*, 6 064067.

[15] X.-D. Fan, L. Zhang, *Physical Review Research* **2021**, *3*, 1 013251.

[16] C. Zhang, W. K. Cao, L. T. Wu, J. C. Ke, Y. Jing, T. J. Cui, Q. Cheng, *Applied Physics Letters* **2021**, *118*, 13 133502.

[17] W. K. Cao, C. Zhang, L. T. Wu, K. Q. Guo, J. C. Ke, T. J. Cui, Q. Cheng, *Physical Review Applied* **2021**, *15*, 2 024026.

[18] Y. Li, B. Liang, Z.-m. Gu, X.-y. Zou, J.-c. Cheng, *Scientific reports* **2013**, *3*, 1 1.

[19] J. Zhao, B. Li, Z. Chen, C.-W. Qiu, *Scientific reports* **2013**, *3*, 1 1.

[20] H.-T. Zhou, W.-X. Fu, Y.-F. Wang, Y.-S. Wang, V. Laude, C. Zhang, *Materials & Design* **2021**, *199* 109414.

[21] Y. Xie, C. Shen, W. Wang, J. Li, D. Suo, B.-I. Popa, Y. Jing, S. A. Cummer, *Scientific reports* **2016**, *6*, 1 1.

[22] Y. Zhu, J. Hu, X. Fan, J. Yang, B. Liang, X. Zhu, J. Cheng, *Nature communications* **2018**, *9*, 1 1.

[23] Y. Zhu, N. J. Gerard, X. Xia, G. C. Stevenson, L. Cao, S. Fan, C. M. Spadaccini, Y. Jing, B. Assouar, *Advanced Functional Materials* **2021**, *31*, 27 2101947.

[24] X. Jiang, Y. Li, B. Liang, J.-c. Cheng, L. Zhang, *Physical review letters* **2016**, *117*, 3 034301.

[25] B.-I. Popa, L. Zigoneanu, S. A. Cummer, *Physical Review B* **2013**, *88*, 2 024303.

[26] X. Chen, X. Xu, S. Ai, H. Chen, Y. Pei, X. Zhou, *Applied Physics Letters* **2014**, *105*, 7 071913.

[27] S. Xiao, G. Ma, Y. Li, Z. Yang, P. Sheng, *Applied Physics Letters* **2015**, *106*, 9 091904.

[28] S. Babaee, J. T. Overvelde, E. R. Chen, V. Tournat, K. Bertoldi, *Science Advances* **2016**, *2*, 11 e1601019.

[29] Y. Li, C. Shen, Y. Xie, J. Li, W. Wang, S. A. Cummer, Y. Jing, *Physical review letters* **2017**, *119*, 3 035501.

[30] G. Ma, X. Fan, P. Sheng, M. Fink, *Proceedings of the National Academy of Sciences* **2018**, *115*, 26 6638.

[31] S.-W. Fan, S.-D. Zhao, L. Cao, Y. Zhu, A.-L. Chen, Y.-F. Wang, K. Donda, Y.-S. Wang, B. Assouar, *Physical Review B* **2020**, *101*, 2 024104.

[32] Y. Zhu, F. Fei, S. Fan, L. Cao, K. Donda, B. Assouar, *Physical Review Applied* **2019**, *12*, 3 034029.

[33] Z. Tian, C. Shen, J. Li, E. Reit, Y. Gu, H. Fu, S. A. Cummer, T. J. Huang, *Advanced functional materials* **2019**, *29*, 13 1808489.

[34] Y. Zhu, L. Cao, A. Merkel, S.-W. Fan, B. Vincent, B. Assouar, *Nature Communications* **2021**, *12*, 1 1.

[35] S. Zuo, C. Cai, X. Li, Y. Tian, E. Liang, *Journal of Physics D: Applied Physics* **2022**.

[36] S.-M. Yuan, A.-L. Chen, X.-Y. Du, H.-W. Zhang, B. Assouar, Y.-S. Wang, *Mechanical Systems and Signal Processing* **2022**, *179* 109371.

[37] H.-W. Dong, C. Shen, S.-D. Zhao, W. Qiu, H. Zheng, C. Zhang, S. A. Cummer, Y.-S. Wang, D. Fang, L. Cheng, *National Science Review* **2022**.

[38] P. Wang, G. Yu, Y. Li, X. Wang, N. Wang, *New Journal of Physics* **2020**, *22*, 2 023006.

[39] X.-D. Fan, Y.-F. Zhu, B. Liang, J. Yang, J. Yang, J.-C. Cheng, *Applied Physics Letters* **2017**, *111*, 10 103502.

[40] X. Fan, X. Huang, Y. Kang, C. Li, N. Li, C. Weng, *Applied Sciences* **2022**, *12*, 6 3025.